Thermal effects on helium scattering from LiF(001) at grazing incidence

L. Frisco and M. S. Gravielle*
Instituto de Astronomía y Física del Espacio (UBA-CONICET), Casilla de Correo 67, Sucursal 28, C1428EGA Buenos Aires, Argentina

(Received 8 October 2020; accepted 10 December 2020; published 23 December 2020)

Grazing-incidence fast atom diffraction (GIFAD) is an exceptionally sensitive method for surface analysis, which can be applied not only at room temperature but also at higher temperatures. In this work we use the He-LiF(001) system as a benchmark to study the influence of temperature on GIFAD patterns from insulator surfaces. Our theoretical description is based on the phonon-surface initial value representation (P0-SIVR) approximation, which is a semiquantum approach that includes the phonon contribution to the elastic scattering. Within the P0-SIVR approach the main features introduced by thermal lattice vibrations on the angular distributions of scattered projectiles are investigated as a function of the crystal temperature. We found that azimuthal and polar spectra are strongly affected by thermal fluctuations, which modify the relative intensities and the polar spread of the interference structures. These findings are relevant for the use of GIFAD in surface research. Moreover, the present results are contrasted with available experimental data at room temperature.

DOI: 10.1103/PhysRevA.102.062821

I. INTRODUCTION

Grazing-incidence fast atom diffraction (GIFAD or FAD) is nowadays considered one of the most powerful nondestructive methods of surface analysis [1,2]. Among the attractive features of the GIFAD technique are its extraordinary sensitivity to the morphological and electronic characteristics of the topmost atomic layer [3,4] and the wide variety of materials that are able to be analyzed, which ranges from insulators [5], semiconductors [6], and metals [7] to adsorbate-covered metal surfaces [8], ultrathin films [9], organic-metal interfaces [10,11], and graphene layers [12]. In addition, even though the vast majority of GIFAD experiments have been carried out at room temperature, GIFAD can also be applied at higher temperatures, like in the case of the molecular beam epitaxial growth of GaAs at temperatures up to 620 °C, which was monitored in real time by means of GIFAD [13]. Precisely, this article focuses on the influence of temperature on GIFAD patterns, an effect that has scarcely been studied in the literature [14–18].

In this paper the temperature dependence of GIFAD is analyzed by considering an insulator surface—LiF—for which thermal lattice vibrations are expected to represent the main decoherence mechanism [19,20]. In particular, we investigate thermal effects on angular distributions of fast He atoms scattered off LiF(001) under axial surface channeling conditions. This system has been extensively investigated with GIFAD at room temperature [16,21–26], becoming a prototype of the GIFAD phenomenon. However, most of the theoretical descriptions have been based on static crystal models [5,6,24,27,28], with the crystal atoms at rest at their equilibrium positions, while thermal vibration effects have been studied to a much lesser extent [14,16–18]. Furthermore, to our knowledge there are no available results of He-LiF GIFAD at temperatures higher than room temperature.

To investigate thermal effects on GIFAD we make use of a recently developed semiquantum approach, named phonon-surface initial value representation (P-SIVR) [29]. The P-SIVR approximation is based on the previous SIVR approach for grazing scattering from a rigid surface [27], incorporating lattice vibrations (i.e., phonon contributions) through a quantum description of the surface given by the harmonic crystal model [30]. The P-SIVR probability is expanded in terms of the number n of phonons exchanged between the crystal and the projectile during the collision. It gives rise to a series of partial Pn -SIVR probabilities involving the exchange of n phonons, where the first-order term—P0-SIVR—corresponds to the elastic scattering without net phonon exchange [29].

P0-SIVR projectile distributions for He-LiF(001) scattering under a fixed incidence condition are here investigated considering temperatures T in the 250–1000 K range. With the goal of determining the contribution of thermal lattice vibrations, P0-SIVR double differential probabilities, as a function of the final azimuthal and polar angles, are contrasted with the angular distribution for a rigid crystal, derived within the SIVR approximation. Also, azimuthal and polar spectra of scattered helium atoms are separately analyzed as a function of T, finding different behaviors along both directions. From polar P0-SIVR profiles for different T values, the log-normal dependence on the final polar angle, proposed in Ref. [14], is examined. Finally, the present P0-SIVR results at room temperature are validated through the comparison with available experimental data [25].

The article is organized as follows. The P0-SIVR approach is summarized in Sec. II, while results are presented and discussed in Sec. III. In Sec. IV we outline our conclusions. Atomic units (a.u.) are used unless otherwise stated.

*Corresponding author: msilvia@iafe.uba.ar

II. THEORETICAL MODEL

Within the P0-SIVR approximation, the effective transition amplitude for atom-surface scattering with initial (final) projectile momentum $\mathbf{K}_i(\mathbf{K}_f)$, without net phonon exchange (i.e., with $K_f = K_i$), reads [29]

$$\mathcal{A}^{(\mathrm{P0-SIVR})} = \int d\mathbf{R}_o\, f(\mathbf{R}_o) \int d\mathbf{K}_o\, g(\mathbf{K}_o) \times \int d\underline{\mathbf{u}}_o\, a_0(\mathbf{R}_o, \mathbf{K}_o, \underline{\mathbf{u}}_o), \tag{1}$$

where the functions f and g describe the position and momentum profiles, respectively, of the incident projectile wave-packet. The function

$$a_0(\mathbf{R}_o, \mathbf{K}_o, \underline{\mathbf{u}}_o) = \int_0^{+\infty} dt\ |J_P(t)|^{1/2} e^{i\nu_t \pi/2}\, \mathcal{V}_c(\mathbf{R}_t) \times \exp\left[i(\varphi_t - \mathbf{Q}\cdot\mathbf{R}_o)\right] \tag{2}$$

represents the partial amplitude corresponding to the classical projectile trajectory $\mathbf{R}_t \equiv \mathbf{R}_t(\mathbf{R}_o, \mathbf{K}_o, \underline{\mathbf{u}}_o)$, which starts at the initial time $t = 0$ in the position $\mathbf{R}_o$ with momentum $\mathbf{K}_o$. This time-dependent projectile position $\mathbf{R}_t$ depends on the spatial configuration $\underline{\mathbf{u}}_o$ of the crystal at $t = 0$, where the underlined vector $\underline{\mathbf{u}}_o$ denotes the $3N$-dimension vector associated with the spatial displacements of the N ions contained in the crystal sample, with respect to their equilibrium positions. In the present model such crystal deviations are considered invariable during the collision time, which is much shorter than the characteristic time of phonon vibrations [30].

In Eq. (2), $J_P(t) = \det\left[\partial\mathbf{R}_t/\partial\mathbf{K}_o\right] = |J_P(t)|\exp(i\nu_t\pi)$ is a Jacobian factor (a determinant), $\mathbf{Q} = \mathbf{K}_f - \mathbf{K}_i$ is the projectile momentum transfer, and

$$\varphi_t = \int_0^t dt' \left[\frac{(\mathbf{K}_f - \mathbf{K}_{t'})^2}{2m_P} - V_{\mathrm{PS}}(\mathbf{R}_{t'}, \underline{\mathbf{u}}_o)\right] \tag{3}$$

is the SIVR phase at the time t [27], where m_P is the projectile mass and $\mathbf{K}_t = m_P d\mathbf{R}_t/dt$ is the classical projectile momentum. The potential $V_{\mathrm{PS}}(\mathbf{R}_{t'}, \underline{\mathbf{u}}_o)$ represents the projectile-surface interaction that governs the classical projectile motion, which depends on the given spatial configuration $\underline{\mathbf{u}}_o$ of the crystal. In this work, V_{PS} is obtained from the pairwise additive model of Ref. [31], reading

$$V_{\mathrm{PS}}(\mathbf{R}_t, \underline{\mathbf{u}}) = \sum_{\mathbf{r}_\mathrm{B}} v_{\mathbf{r}_\mathrm{B}}(\mathbf{R}_t - \mathbf{r}_\mathrm{B} - \mathbf{u}(\mathbf{r}_\mathrm{B})), \tag{4}$$

where $\mathbf{u}(\mathbf{r}_\mathrm{B})$ denotes the spatial deviation of the crystal atom with equilibrium position $\mathbf{r}_\mathrm{B}$ and the summation on $\mathbf{r}_\mathrm{B}$ covers all the occupied Bravais-lattice sites. The potential $v_{\mathbf{r}_\mathrm{B}}(\mathbf{r})$ describes the binary interaction between the projectile and the crystal ion corresponding to the lattice site $\mathbf{r}_\mathrm{B}$ as a function of the relative vector $\mathbf{r}$, with $v_{\mathbf{r}_\mathrm{B}} = v_1$ or v_2 to consider the two different ions of the crystallographic basis. Hence, in Eq. (2) the crystal factor $\mathcal{V}_c(\mathbf{R}_t)$ can be expressed as

$$\mathcal{V}_c(\mathbf{R}_t) = \int d\mathbf{q} \sum_{\mathbf{r}_\mathrm{B}} \tilde{v}_{\mathbf{r}_\mathrm{B}}(\mathbf{q}) \exp[-W_{\mathbf{r}_\mathrm{B}}(\mathbf{q})] \times \exp\left[i\mathbf{q}\cdot(\mathbf{R}_t - \mathbf{r}_\mathrm{B})\right], \tag{5}$$

with $\tilde{v}_{\mathbf{r}_\mathrm{B}}(\mathbf{q})$ denoting the Fourier transform of $v_{\mathbf{r}_\mathrm{B}}$ and $W_{\mathbf{r}_\mathrm{B}}(\mathbf{q})$ being the momentum-dependent Debye-Waller function. This latter function is defined as

$$W_{\mathbf{r}_\mathrm{B}}(\mathbf{q}) = \langle[\mathbf{q}\cdot\mathbf{u}(\mathbf{r}_\mathrm{B})]^2\rangle/2, \tag{6}$$

where the dependence on $\mathbf{r}_\mathrm{B}$ indicates that its value changes for the different species of the crystallographic basis, as well as for bulk or surface positions.

The P0-SIVR probability for scattering in the direction of the solid angle $\Omega_f = (\theta_f, \varphi_f)$ is obtained from Eq. (1) as

$$\frac{dP^{(\mathrm{P0-SIVR})}}{d\Omega_f} = K_f^2 |\mathcal{A}^{(\mathrm{P0-SIVR})}|^2, \tag{7}$$

where θ_f is the final polar angle, measured with respect to the surface, and φ_f is the azimuthal angle, measured with respect to the axial channel. The interested reader can find the steps and assumptions involved in the derivation of the P0-SIVR approximation in the Appendix of Ref. [29].

III. RESULTS

In this article ^{4}He atoms grazingly colliding with a LiF(001) surface along the ⟨110⟩ channel (with width $a_y = 5.4$ a.u.) are used as a benchmark to investigate thermal effects on GIFAD patterns. For this purpose we applied the P0-SIVR approach to evaluate final helium distributions, as given by Eq. (7), considering different temperatures T of the LiF sample. Temperatures are confined to the 250–1000 K range, for which a linear T dependence of the mean-square vibrational amplitudes of the crystal ions can be assumed [32].

During the work we kept a fixed incidence condition, given by the impact energy $E = K_i^2/(2m_P) = 1.25$ keV and the incidence angle $\theta_i = 1.1^\circ$. (measured with respect to the surface plane). It corresponds to the normal incidence energy $E_\perp = E\sin^2\theta_i = 0.46$ eV, associated with the projectile motion perpendicular to the axial direction. In our theoretical model we consider that before impinging on the LiF surface, the atomic beam is collimated by a square slit of size d, placed at a distance L from the surface [33]. Like in GIFAD experiments [34], within the P0-SIVR and SIVR models [35] the azimuthal width of the interference patterns depends on the number $N_i \simeq 2\pi/\sqrt{m_P E} \times L/(da_y)$ of equivalent parallel channels that are coherently illuminated by the atomic beam, decreasing as N_i augments [27,33]. In turn, the polar spread of the patterns varies with d/L [36], while the shape of the collimating slit plays a secondary role [35]. Therefore, except for the experimental comparison (Sec. III D), in all the cases we used the same collimating parameters, which were chosen as $d = 0.09$ mm and $L = 36$ cm. The angular dispersion of the beam was 0.006°. These values correspond to an extremely good collimating condition, in accord with current experimental setups for GIFAD [37].

The transition amplitude $\mathcal{A}^{(\mathrm{P0-SIVR})}$ was calculated from Eq. (1) by using the spatial and momentum wave-packet profiles defined in Refs. [33,35]. The integral on $\mathbf{R}_o$ was evaluated considering that all the classical trajectories start at the same distance from the surface, chosen as equal to the lattice constant, for which the projectile is hardly affected by the surface interaction [31]. Also, the integral on $\mathbf{K}_o$ was reduced to a two-dimensional integral over the solid angle $\Omega_o = (\theta_o, \varphi_o)$ that

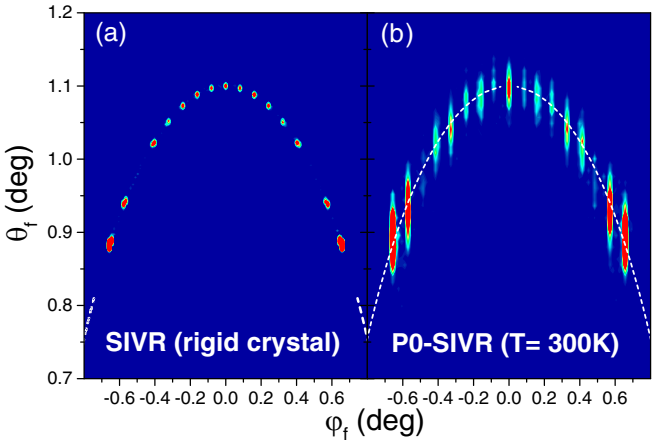

FIG. 1. Two-dimensional projectile distributions, as a function of θ_f and φ_f, for 1.25 keV ^{4}He atoms scattered off LiF(001) at the temperature $T = 300$ K. Incidence along the ⟨110⟩ channel with the grazing angle $\theta_i = 1.1^\circ$ is considered. Results derived within (a) the SIVR approximation, for a rigid crystal, and (b) the P0-SIVR approach, including thermal vibrations, are displayed.

determines the $\mathbf{K}_o$ orientation, with $K_o = K_i$ accounting for the negligible energy dispersion of the incident beam [33,34].

Within the P0-SIVR approach, thermal effects come from the integral on $\underline{\mathbf{u}}_o$, involved in Eq. (1), as well as from the Debye-Waller factor $\exp[-W_{\mathbf{r}_B}(\mathbf{q})]$ which acts as an effective screening in $\mathcal{V}_c(\mathbf{R}_t)$ [Eq. (5)]. The Debye-Waller function was approximated as $W_{\mathbf{r}_B}(\mathbf{q}) \simeq q^2\langle \mathbf{u}(\mathbf{r}_B)^2\rangle/2$, while the integral on $\underline{\mathbf{u}}_o$ was evaluated with the Monte Carlo technique by considering randomly displaced ion positions obtained from independent Gaussian distributions with mean-square vibrational amplitudes $\langle \mathbf{u}(\mathbf{r}_B)^2\rangle$. For the LiF crystal at a given temperature T, the mean-square vibrational amplitudes $\langle \mathbf{u}(\mathbf{r}_B)^2\rangle_T$ were derived from the corresponding values for the reference temperature $T_{\rm ref} = 300$ K, which were extracted from Ref. [16]. Such reference values, which take into account the differences between the two ionic species and between bulk and surface (topmost layer) sites, were then extrapolated as a function of T following the temperature dependence given in Ref. [32]. That is, we approximate $\langle \mathbf{u}(\mathbf{r}_B)^2\rangle_T \approx [1 + B(\mathbf{r}_B)(T/T_{\rm ref} - 1)]\langle \mathbf{u}(\mathbf{r}_B)^2\rangle_{T_{\rm ref}}$, with $B(\mathbf{r}_B) = 0.795$ (0.890) for Li (F) ions.

A. Thermal effects on the (θ_f, φ_f) distributions

Since GIFAD experiments involving insulator surfaces are usually carried out at room temperature, we start analyzing thermal effects at $T = 300$ K. In Fig. 1 the P0-SIVR two-dimensional (2D) distribution as a function of the final scattering angles θ_f and φ_f, for a lithium fluoride surface at $T = 300$ K, is displayed along with the angular distribution derived within the SIVR approach, which assumes an ideal LiF crystal with its ions at rest at their equilibrium positions [27]. While the SIVR distribution [Fig. 1(a)] presents nearly circular spots associated with equally φ_f-spaced Bragg maxima (with order m, $m = 0, \pm1, \pm2, \ldots$), the phonon contribution included in the P0-SIVR approximation transforms such Bragg peaks into elongated strips, as shown in Fig. 1(b).

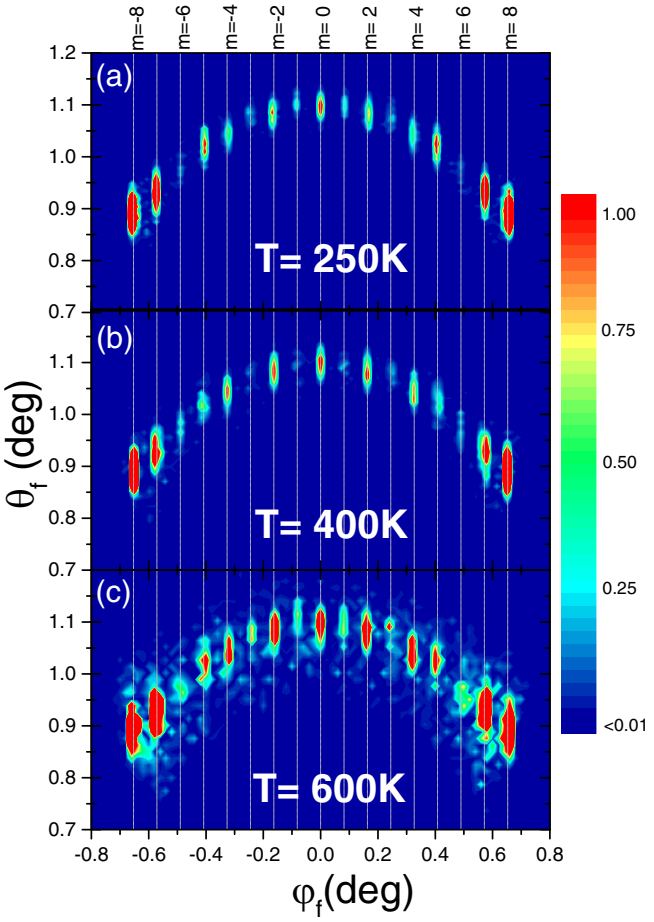

FIG. 2. Analogous to Fig. 1(b) for three different temperatures: (a) $T = 250$ K, (b) $T = 400$ K, and (c) $T = 600$ K. In every panel, the intensity scale is normalized to the maximum intensity. Vertical dashed lines denote the ideal Bragg-peak positions with their orders m indicated in the upper axis.

Moreover, in the absence of lattice vibrations the Bragg maxima of Fig. 1(a) lie on a circle of radius θ_i (the Laue circle), which is a sign of elastic scattering from an ideal surface under extremely good collimating conditions [33,38]. But when thermal fluctuations of the crystal lattice are taken into account, as happens in the P0-SIVR distribution of Fig. 1(b), the maximum intensity of some Bragg orders appears at a polar angle slightly shifted above or below the Laue circle, as is usually observed in GIFAD experiments [1].

In order to investigate how the previous effects change with the temperature, in Fig. 2 we display 2D angular distributions derived with the P0-SIVR approach for LiF crystals at different temperatures: (a) $T = 250$ K, (b) $T = 400$ K, and (c) $T = 600$ K. In every panel, the intensity scale was normalized at the maximum intensity of the GIFAD distribution, which corresponds to the outermost peak associated with rainbow scattering. Analogous intensity scales were considered in the other P0-SIVR distributions shown in the article. From Fig. 2 it is evident that the azimuthal positions of the Bragg maxima are independent of T, being completely determined by the crystallographic parameters of the ideal surface [1]. Furthermore, the three P0-SIVR distributions of Fig. 2 look

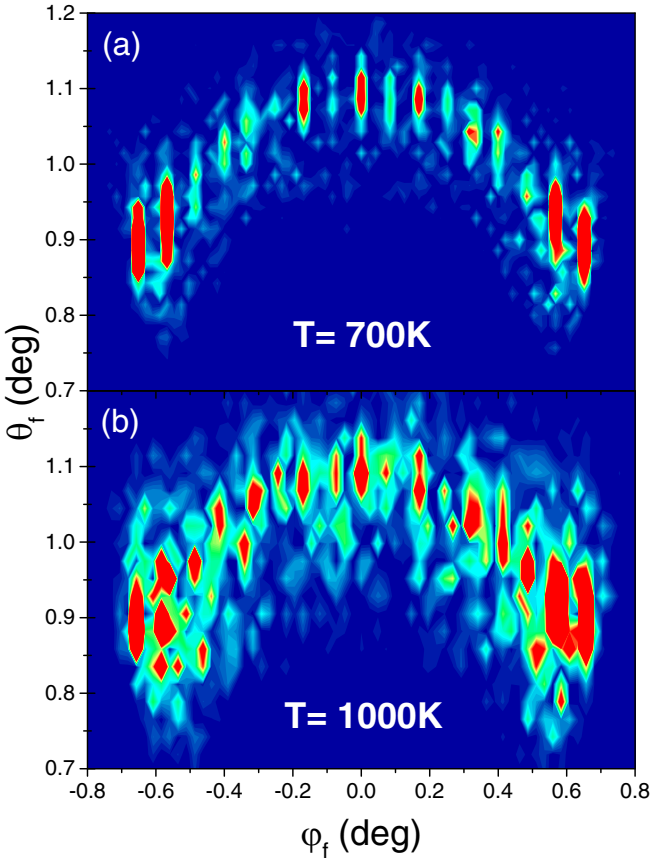

FIG. 3. Analogous to Fig. 1(b) for (a) $T = 700$ K and (b) $T = 1000$ K. The intensity scale is similar to that in Fig. 2.

similar to each other, displaying intense $m = 0$ (central) and $m = \pm 2$ maxima, along with almost suppressed $m = \pm 1, \pm 3$, and ± 6 peaks. But in spite of this overall similitude, we found that the relative intensities and the polar spread of the Bragg maxima depend on the temperature, the latter increasing as T augments. Note that GIFAD structures are clearly visible even for a temperature as high as $T = 600$ K, although they start to blur at this temperature. This fact is in accord with the experiments for semiconductor surfaces [6,13], where GIFAD patterns were observed at high temperatures.

For the He-LiF(001) system, GIFAD patterns gradually smudge as the temperature rises above 700 K, ending up almost completely blurred for LiF at $T = 1000$ K, for which thermal vibrations strongly deteriorate the coherence, as observed in Fig. 3. Besides, the intensity of the interference structures decreases sharply as the temperature increases, being about 2 orders of magnitude lower at $T = 700$ K than at room temperature. This fact might contribute to making their experimental detection difficult in this high-T range.

A more in-depth inspection of the aforementioned thermal effects along the azimuthal and polar directions is presented in Secs. III B and III C, respectively.

B. Influence of T on the azimuthal spectra

Surface characterization by means of GIFAD is commonly based on the theory-experiment comparison of the relative

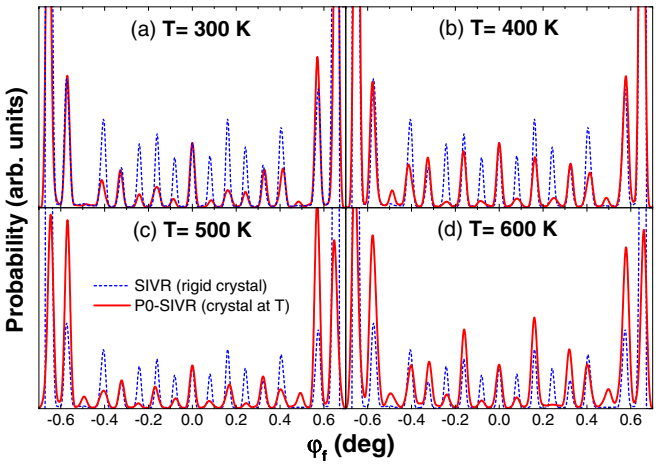

FIG. 4. Differential probability $dP^{(\mathrm{P0-SIVR})}/d\varphi_f$, as a function of the azimuthal angle φ_f, for the case of Fig. 1 considering different crystal temperatures: (a) $T = 300$ K, (b) $T = 400$ K, (c) $T = 500$ K, and (d) $T = 600$ K. In all the panels, the red solid line denotes the P0-SIVR probability including thermal vibrations, and the blue dashed line denotes the SIVR probability for a rigid crystal.

intensities of the interference maxima along the transverse direction, perpendicular to the incidence channel [5,6]. Therefore, to use GIFAD as a surface analysis tool it is important to know the influence of temperature on such transverse spectra, i.e., on the azimuthal projectile distributions. In Fig. 4 we plot $dP^{(\mathrm{P0-SIVR})}/d\varphi_f$, as a function of the azimuthal angle φ_f, for temperatures varying between 300 and 600 K. These single differential probabilities were calculated by integrating Eq. (7) over a reduced annulus of mean radius θ_i and central thickness 0.03°, as is usually done to derive the experimental projected intensities [1,38]. In all the panels P0-SIVR results including thermal lattice fluctuations are contrasted with the azimuthal distribution for an ideal rigid LiF crystal, derived within the SIVR approach, normalizing both spectra at $\varphi_f = 0$. From Fig. 4 we confirm that not only are the φ_f positions of the Bragg peaks independent of T but also the azimuthal widths of these maxima are weakly affected by thermal vibrations, being mainly determined by the number N_i of parallel channels coherently illuminated by the atomic beam [34,35]. On the contrary, the relative intensities of the Bragg peaks are affected by the lattice fluctuations, which strongly suppress the intensities corresponding to the $m = \pm 1$ and ± 3 Bragg orders, this fact being observed for all the T values. Hence, this suppression effect might be used to determine the lattice vibration contribution in the studied case.

C. Influence of T on the polar profiles

An important feature introduced by the thermal vibrations is the θ_f dispersion of the GIFAD patterns, which transforms the punctual spots produced by the rigid crystal into vertical streaks, as observed in Fig. 1. With the aim of analyzing the dependence on T of such a polar-angle spread, in Fig. 5 we display the polar profile of the central maximum, that is, the differential probability $dP^{(\mathrm{P0-SIVR})}/d\theta_f$ at $\varphi_f = 0$, as a function of the polar angle θ_f, for the same temperatures as in Fig. 4. In each panel, P0-SIVR results including phonon

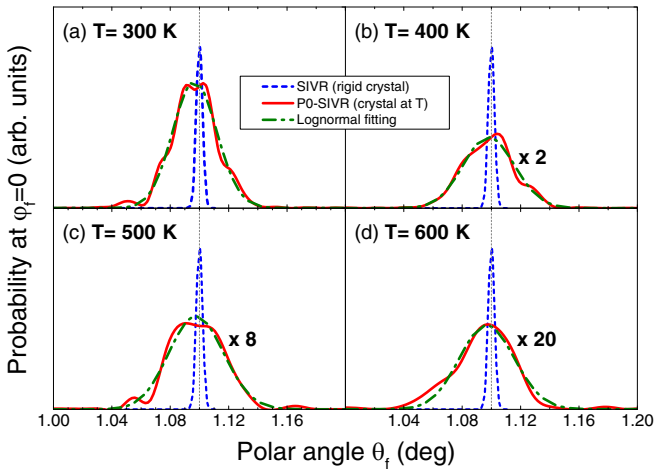

FIG. 5. Intensity profile of the central maximum at $\varphi_f = 0$, as a function of the polar angle θ_f, for the case of Fig. 1, considering different temperatures: (a) $T = 300$ K, (b) $T = 400$ K, (c) $T = 500$ K, and (d) $T = 600$ K. In all the panels, the red solid line denotes the differential probability derived within the P0-SIVR approach, the blue dashed line denotes the SIVR probability for a rigid crystal, and the green dot-dashed line denotes the fitting of P0-SIVR results by means of a log-normal distribution, as given by Eq. (8). The vertical gray dashed line denotes the ideal θ_f position on the Laue circle (i.e., $\theta_f = \theta_i$).

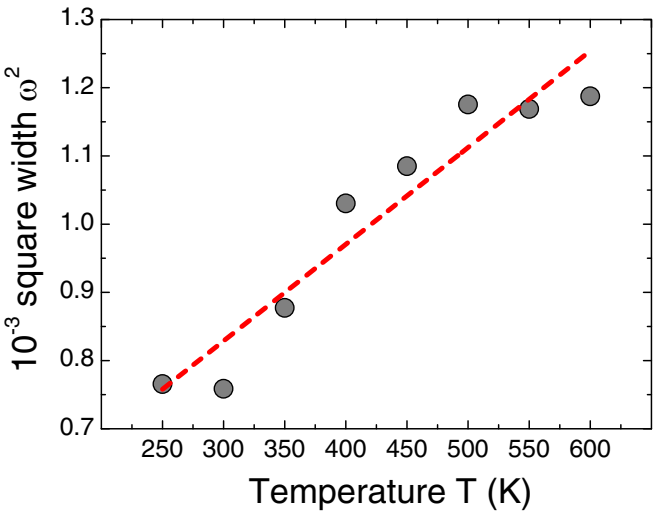

FIG. 6. Square width ω^2 of the distribution given by Eq. (8), as a function of the temperature. Circles show the values derived by fitting P0-SIVR results; the red dashed line shows the linear fitting of the present ω^2 values.

contributions are compared with the SIVR profile corresponding to a rigid crystal. In contrast with the SIVR spectrum, which presents a sharp peak centered at the specular reflection angle (i.e., $\theta_f = \theta_i$), the polar distribution derived within the P0-SIVR approach shows a broad maximum, whose intensity decreases as T increases. This latter effect is only partially due to the screening of the projectile-surface interaction introduced by the Debye-Waller factor in Eq. (5). Additionally, in Fig. 5 we observe that the width of the P0-SIVR peak is affected by the thermal fluctuations, showing a slight increase as the temperature augments.

Similar thermal spread of the polar angle θ_f was predicted by Manson *et al.* in Ref. [14], where the polar profile of the GIFAD patterns was estimated as following a log-normal distribution. In fact, such a log-normal distribution has been previously proposed in Refs. [39,40]. In order to verify this behavior, we fit the θ_f profiles at $\varphi_f = 0$ derived with the P0-SIVR approach for different T values with the log-normal function

$$\mathcal{P}(\theta_f) = \frac{A}{\omega\,\theta_f} \exp\left[\frac{-2[\ln(\theta_f/\theta_c)]^2}{\omega^2}\right], \tag{8}$$

where A, θ_c, and ω are fitting parameters that depend on T. The resulting $\mathcal{P}(\theta_f)$ functions, displayed with green dot-dashed lines in Fig. 5, reproduce the P0-SIVR curves quite well, allowing us to determine the width ω of the effective log-normal distribution of Eq. (8) as a function of T.

Within the log-normal model of Ref. [14], the square width of the distribution given by $\mathcal{P}(\theta_f)$ is obtained as proportional to the mean-square vibrational amplitude normal to the surface plane. That is, $\omega^2 = \Gamma^2 \langle u_z^2 \rangle_T$, where the coefficient of proportionality Γ coincides with the normalized slope of the projectile-surface potential, which is assumed as $V_0 \exp(-\Gamma Z)$ in Ref. [14], with Z being the distance to the surface. Then, to test this relation, in Fig. 6 we plot ω^2 values obtained by means of the log-normal fitting of Eq. (8) for different temperatures T in the 250–600 K range. Even though the points of Fig. 6 show an appreciable dispersion, they seem to follow a linear tendency, leading to a rate of $\Gamma \approx 0.22$ Å^{-1}. But this Γ value is 1 order of magnitude smaller than the normalized slope of the projectile-surface potential around the turning point, $-[V_{PS}(Z)]^{-1} dV_{PS}/dZ$, in contrast with the prediction by the log-normal model [14]. This difference might be associated with the influence of soft potential effects [5,37], which are not taken into account within the model of Ref. [14] that is based on a planar potential along with a hard corrugated wall (i.e., only at the classical turning point) description [41].

D. Experimental comparison

Finally, we check the validity of present results for the He-LiF(001) system by contrasting double differential P0-SIVR probabilities with experimental data extracted from Ref. [25], which were measured at room temperature, i.e., at $T = 300$ K. In Fig. 7, 2D angular distributions as a function of θ_f and φ_f, derived from the P0-SIVR and SIVR approaches, are compared with the experimental intensity distribution as recorded with a position-sensitive detector [25]. In this case, P0-SIVR and SIVR simulations were done by assuming an atomic beam collimated through a square slit of size $d = 0.3$ mm, placed at a distance of $L = 25$ cm from the surface. Although details about the collimation setup were not provided in Ref. [25], the chosen collimating parameters agree with those reported in other articles by the same group [34].

From Fig. 7, the P0-SIVR distribution shows a good accord with the experimental data, both presenting a central region with even Bragg orders much higher than the odd ones. Instead, the relative intensities of the Bragg peaks provided by the SIVR approximation differ from the former, showing

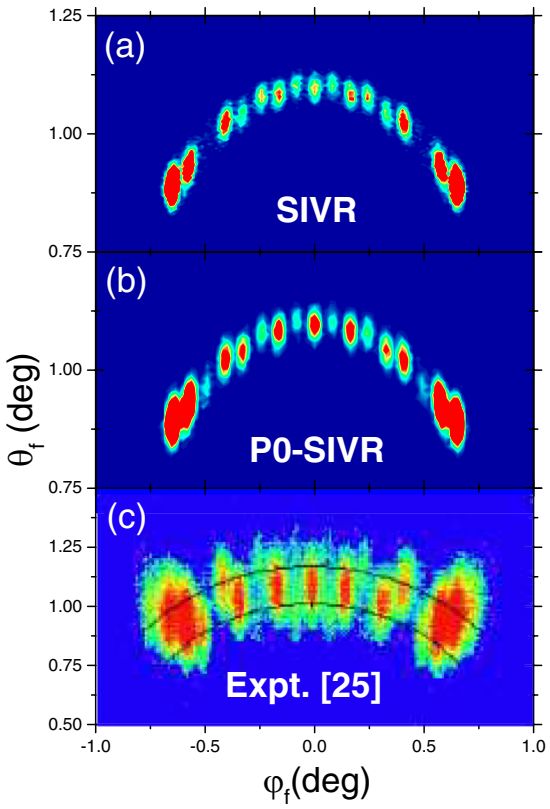

FIG. 7. Two-dimensional projectile distribution, as a function of θ_f and φ_f, for the case of Fig. 1. Results are derived within (a) the SIVR approach for a rigid crystal and (b) the P0-SIVR approximation, including thermal lattice vibrations, both with the collimating parameters given in Sec. III D. (c) Experimental data extracted from Ref. [25].

a less pronounced intensity contrast between even and odd Bragg orders around the axial direction. In addition, in a fashion similar to that of Fig. 1, the effect of thermal fluctuations gives rise to an increase of the polar spread of the P0-SIVR patterns, with respect to that of the SIVR distribution. However, note that the P0-SIVR distribution [Fig. 7(b)] has a θ_f dispersion smaller than that of the experiment [Fig. 7(c)]. Also, in the azimuthal direction, the experimental peaks of Fig. 7(c) show a more extended distribution than the P0-SIVR maxima. As discussed in recent works [17,42], this suggests that the polar and azimuthal spreads of the experimental Bragg peaks have additional contributions due to inelastic processes involving phonon transitions, which are not included in the present model. This inelastic effect is expected to be more pronounced as $E_\perp$ increases and, consequently, the projectile moves closer to the surface.

IV. CONCLUSIONS

In this work the influence of temperature on GIFAD patterns for the He-LiF(001) system has been studied by using the P0-SIVR approximation. The P0-SIVR approach is a semiquantum method that describes zero-phonon scattering including the contribution of thermal lattice vibrations. These thermal vibrations were found to be responsible for the polar spread of the diffraction patterns, which transforms the sharp Bragg maxima produced by the rigid crystal into vertical streaks. Furthermore, P0-SIVR spectra as a function of the azimuthal angle vary with the temperature, which strongly modifies the relative intensity of the diffraction maxima, while the azimuthal width of the peaks is slightly affected by the thermal lattice fluctuations. As happens for semiconductor surfaces, well-defined GIFAD patterns are obtained for temperatures as high as 600 K. In addition, by analyzing the polar profile of the central Bragg maximum as a function of T, the log-normal behavior proposed in Ref. [14] was also scrutinized. We found that the square width ω^2 of the *effective* log-normal distribution roughly increases linearly with the crystal temperature, but the slope is much lower than that estimated in Ref. [14] from a simple potential model.

The present P0-SIVR results were contrasted with the experimental projectile distribution from Ref. [25], showing an overall good agreement. Nevertheless, the polar extension of the experimental pattern, as well as the azimuthal width of the peaks, is underestimated by the P0-SIVR description, suggesting that other effects, like phonon excitations or surface defects, might contribute to the angular dispersion of GIFAD patterns at room temperature. Therefore, an exhaustive experimental study of the T dependence of GIFAD from insulator surfaces should be desirable.

ACKNOWLEDGMENT

The authors acknowledge financial support from CONICET (PIP 2014-11220130100386CO) and ANPCyT (PICT-2017-1201 and PICT-2017-2945) of Argentina.

[1] H. Winter and A. Schüller, Fast atom diffraction during grazing scattering from surfaces, Prog. Surf. Sci. **86**, 169 (2011).

[2] M. Debiossac, P. Atkinson, A. Zugarramurdi, M. Eddrief, F. Finocchi, V. H. Etgens, A. Momeni, H. Khemliche, A. G. Borisov, and P. Roncin, Fast atom diffraction inside a molecular beam epitaxy chamber, a rich combination, Appl. Surf. Sci. **391**, 53 (2017).

[3] J. Seifert and H. Winter, Quantitative structure determination using grazing scattering of fast atoms: Oxygen-induced missing-row reconstruction of Mo(112), Phys. Rev. B **93**, 205417 (2016).

[4] M. del Cueto, A. S. Muzas, M. F. Somers, G. J. Kroes, C. Díaz, and F. Martín, Exploring surface landscapes with molecules: Rotatonally induced diffraction of H_2 on LiF(001) under fast grazing incidence conditions, Phys. Chem. Chem. Phys. **19**, 16317 (2017).

[5] A. Schüller, D. Blauth, J. Seifert, M. Busch, H. Winter, K. Gärtner, R. Włodarczyk, J. Sauer, and M. Sierka, Fast atom

diffraction during grazing scattering from a MgO(001) surface, Surf. Sci. **606**, 161 (2012).

[6] M. Debiossac, A. Zugarramurdi, H. Khemliche, P. Roncin, A. G. Borisov, A. Momeni, P. Atkinson, M. Eddrief, F. Finocchi, and V. H. Etgens, Combined experimental and theoretical study of fast atom diffraction on the $\beta_2(2\times4)$ reconstructed GaAs(001) surface, Phys. Rev. B **90**, 155308 (2014).

[7] C. A. Ríos Rubiano, G. A. Bocan, M. S. Gravielle, N. Bundaleski, H. Khemliche, and P. Roncin, *Ab initio* potential for the He-Ag(110) interaction investigated using grazing-incidence fast-atom diffraction, Phys. Rev. A **87**, 012903 (2013).

[8] A. Schüller, M. Busch, S. Wethekam, and H. Winter, Fast Atom Diffraction from Superstructures on a Fe(110) Surface, Phys. Rev. Lett. **102**, 017602 (2009).

[9] J. Seifert, A. Schüller, H. Winter, R. Włodarczyk, J. Sauer, and M. Sierka, Diffraction of fast atoms during grazing scattering from the surface of an ultrathin silica film on Mo(112), Phys. Rev. B **82**, 035436 (2010).

[10] J. Seifert, M. Busch, E. Meyer, and H. Winter, Surface Structure of Alanine on Cu(110) Studied by Fast Atom Diffraction, Phys. Rev. Lett. **111**, 137601 (2013).

[11] A. Momeni, E. M. Staicu Casagrande, A. Dechaux, and H. Khemliche, Ultrafast crystallization dynamics at an organic-inorganic interface revealed in real time by grazing incidence fast atom diffraction, J. Phys. Chem. Lett. **9**, 908 (2018).

[12] A. Zugarramurdi, M. Debiossac, P. Lunca-Popa, A. J. Mayne, A. Momeni, A. G. Borisov, Z. Mu, P. Roncin, and H. Khemliche, Determination of the geometric corrugation of graphene on SiC(0001) by grazing incidence fast atom diffraction, Appl. Phys. Lett. **106**, 101902 (2015).

[13] P. Atkinson, M. Eddrief, V. H. Etgens, H. Khemliche, M. Debiossac, A. Momeni, M. Mulier, B. Lalmi, and P. Roncin, Dynamic grazing incidence fast atom diffraction during molecular beam epitaxial growth of GaAs, Appl. Phys. Lett. **105**, 021602 (2014).

[14] J. R. Manson, H. Khemliche, and P. Roncin, Theory of grazing incidence diffraction of fast atoms and molecules from surfaces, Phys. Rev. B **78**, 155408 (2008).

[15] F. Aigner, N. Simonović, B. Solleder, L. Wirtz, and J. Burgdörfer, Suppression of Decoherence in Fast-Atom Diffraction at Surfaces, Phys. Rev. Lett. **101**, 253201 (2008).

[16] A. Schüller, S. Wethekam, D. Blauth, H. Winter, F. Aigner, N. Simonović, B. Solleder, J. Burgdörfer, and L. Wirtz, Rumpling of LiF(001) surface from fast atom diffraction, Phys. Rev. A **82**, 062902 (2010).

[17] P. Roncin and M. Debiossac, Elastic and inelastic diffraction of fast atoms, Debye-Waller factor, and Mössbauer-Lamb-Dicke regime, Phys. Rev. B **96**, 035415 (2017).

[18] P. Rousseau, H. Khemliche, N. Bundaleski, P. Soulisse, A. Momeni, and P. Roncin, Surface analysis with grazing incidence fast atom diffraction (GIFAD), J. Phys.: Conf. Ser. **133**, 012013 (2008).

[19] A. Al Taleb, G. Anemone, W. W. Hayes, J. R. Manson, and D. Farías, Multiphonon excitation and quantum decoherence in neon scattering from solid surfaces, Phys. Rev. B **95**, 075414 (2017).

[20] M. C. Schram and E. J. Heller, Approach to coherent interference fringes in helim-surface scattering, Phys. Rev. A **98**, 022137 (2018).

[21] A. Schüller, S. Wethekam, and H. Winter, Diffraction of Fast Atomic Projectiles during Grazing Scattering from a LiF(001) Surface, Phys. Rev. Lett. **98**, 016103 (2007).

[22] P. Rousseau, H. Khemliche, A. G. Borisov, and P. Roncin, Quantum Scattering of Fast Atoms and Molecules on Surfaces, Phys. Rev. Lett. **98**, 016104 (2007).

[23] A. Schüller and H. Winter, Supernumerary Rainbows in the Angular Distribution of Scattered Projectiles for Grazing Collisions of Fast Atoms with a LiF(001) Surface, Phys. Rev. Lett. **100**, 097602 (2008).

[24] A. Schüller, H. Winter, M. S. Gravielle, J. M. Pruneda, and J. E. Miraglia, He-LiF surface interaction potential from fast atom diffraction, Phys. Rev. A **80**, 062903 (2009).

[25] A. Schüller and H. Winter, Difraction of fast atoms under axial surface channeling conditions, Nucl. Instrum. Methods Phys. Res. Sect. B **267**, 628 (2009).

[26] H. Winter, Fast atom diffraction IBA in the regime of quantum scattering, Nucl. Instrum. Methods Phys. Res. Sect. B **332**, 195 (2014).

[27] M. S. Gravielle and J. E. Miraglia, Semiquantum approach for fast atom diffraction: Solving the rainbow divergence, Phys. Rev. A **90**, 052718 (2014).

[28] A. S. Muzas, M. del Cueto, F. Gatti, M. F. Somers, G. J. Kroes, F. Martín, and C. Díaz, H2/LiF(001) diffractive scattering under fast grazing incidence using a DFT-based potential energy surface, Phys. Rev. B **96**, 205432 (2017).

[29] L. Frisco and M. S. Gravielle, Phonon contribution in grazing-incidence fast atom diffraction from insulator surfaces, Phys. Rev. A **100**, 062703 (2019).

[30] N. W. Ashcroft and N. D. Mermin, *Solid State Physics* (Brooks-Cole, Belmont, MA, 1976), Chap. 23.

[31] J. E. Miraglia and M. S. Gravielle, Reexamination of the interaction of atoms with a LiF(001) surface, Phys. Rev. A **95**, 022710 (2017).

[32] R. K. Gupta, Mean-square amplitudes of vibration for ionic crystals, Phys. Rev. B **12**, 4452 (1975).

[33] M. S. Gravielle and J. E. Miraglia, Influence of beam collimation on fast-atom diffraction studied via a semiquantum approach, Phys. Rev. A **92**, 062709 (2015).

[34] J. Seifert, J. Lienemann, A. Schüller, and H. Winter, Studies on coherence and decoherence in fast atom diffraction, Nucl. Instrum. Methods Phys. Res. Sect. B **350**, 99 (2015).

[35] M. S. Gravielle, J. E. Miraglia, and L. Frisco, Coherence-length effects in fast atom diffraction at grazing incidence, Atoms **6**, 64 (2018).

[36] M. S. Gravielle and J. E. Miraglia, Single- and double-slit collimating effects on fast-atom diffraction spectra, Nucl. Instrum. Methods Phys. Res. Sect. B **382**, 42 (2016).

[37] G. A. Bocan, H. Breiss, S. Szilasi, A. Momeni, E. M. Staicu Casagrande, M. S. Gravielle, E. A. Sánchez, and H. Khemliche, Anomalous KCl(001) Surface Corrugation from Fast He Diffraction at Very Grazing Incidence, Phys. Rev. Lett. **125**, 096101 (2020).

[38] M. Debiossac and P. Roncin, Image processing for grazing incidence fast atom diffraction, Nucl. Instrum. Methods Phys. Res. Sect. B **382**, 36 (2016).

[39] K. Cordier, H. Khemliche, and P. Roncin, LCAM-CNRS Report, 2000 (unpublished).

[40] J. Villette, Ph.D. thesis, Université de Paris-Sud, France, 2000, http://tel.archives-ouvertes.fr/tel-00106816/en/.

[41] U. Garibaldi, A. C. Levi, R. Spadacini, and G. E. Tommei, Quantum theory of atom-surface scattering: Diffraction and rainbow, Surf. Sci. **48**, 649 (1975).

[42] M. Debiossac, P. Pan, and P. Roncin, Grazing incidence fast atom diffraction: Similarities and differences with thermal energy atom scattering (TEAS), Phys. Chem. Chem. Phys. (2020).